A new method based on TGA/FTIR coupling to quantify the different thermal degradation steps of EVA/HNT composites prepared by different processing

Amandine Viretto, E. Jasinski, Dominique Lafon-Pham, Belkacem Otazaghine, Rodolphe Sonnier, A. Taguet

A new method based on TGA/FTIR coupling to quantify the different thermal degradation steps of EVA/HNT composites prepared by different processing

A. Viretto [a], E. Jasinski [b], D. Lafon-Pham [c], B. Otazaghine [a], R. Sonnier [a], A. Taguet [a,*]

[a] Polymers Composites and Hybrids (PCH), IMT Mines Alès, 6 avenue de Clavières, F-30319 Alès cedex, France
[b] Université de Lyon, CNRS, Université Claude Bernard Lyon1, INSA de Lyon, Université Jean Monnet, UMR 5223, F-69622 Villeurbanne, France
[c] EUROMOV DHM, Univ Montpellier, IMT Ales, Alès, France

A B S T R A C T

The aim of the present article is to expose a new method based on TGA-FTIR coupling to quantify the different steps of the thermal degradation of EVA in the presence of HNT. Moreover, this quantification of the thermal degradation was also correlated to the color change. EVA/HNT composites were processed with different pro-cessing conditions: solvent casting in THF or melt blending at different temperatures. The HNT fillers content (from 10 wt% up to 30 wt%) and the melt blending temperature (at 130 °C, 150 °C, 170 °C and 190 °C) were varied. The thermal degradation of EVA in the presence of HNT presents three noticeable steps as evidenced by TG analysis: *i)* P_1, which was identified as the catalytic degradation of vinyl acetate (VA) part of EVA occurring during the heating ramp (around 250 °C), *ii)* P_2, which is the main degradation of VA (around 350 °C) and *iii)* P_3, which is the degradation of the polyethylene chain of EVA (around 500 °C). Nevertheless, in the case of melt blended EVA/HNT composites, macroscopic changes (strong smell and browning color) indicate a thermal degradation occurring during the melt blending process, namely P_0. FTIR-TGA coupling allows to quantify the contribution of P_0, P_1 and P_2 (thermal degradation of VA units of EVA) using Gram Schmidt curves of released acetic acid gas which are obtained from the C═$O_{ac.}$ band of acetic acid at 1795 cm^{-1}. The contribution of each thermal degradation step of the VA part of EVA (named P_0 to P_2) was then quantified and reported as A_0 to A_2, respectively. The blending process (solvent or melt) such as the HNT fillers content and the melt blending temperatures have a significant influence on the EVA thermal degradation catalyzed by HNT. For example, it was shown that the thermal degradation of VA units occurring during the processing of EVA+ 30HNT composite (named A_0 and catalyzed by the HNT) was of 40% for melt blending process (at 170 °C), whereas it was close to 0% for solvent casting process. Moreover, the macroscopic changes were evaluated by color measurements and an interesting correlation could be made between A_0 and ΔE* which is the total color deviation. When a sig-nificant catalytic effect, during the melt process was observed (A_0 values higher than 5%), the total color de-viation ΔE* was increased linearly with A_0. Finally, in order to avoid the catalytic effect of HNT on the EVA thermal degradation, a functionalization strategy has been developed with an organosilane leading to the sup-pression of P_1, the catalytic degradation of VA in TG analyses.

Keywords:
Halloysite nanotubes
EVA
Catalytic effect
Quantitative approach
Color measurement

1. Introduction

In recent years, nanocomposite materials have attracted considerable attention while they can provide a significant improvement in terms of physical, mechanical and thermal properties of materials at very low filler content without affecting their processability [1], [2]. The most commonly known layered silicates have been recognized as an interesting resource due to their unique characteristics coupling with their sustainability and low cost [3–5]. Clay minerals are hydrated aluminum phyllosilicates, sometimes containing variable amounts of iron, magnesium, alkali metals, alkaline earths and other cations [5]. Their effective reinforcing effect has been attributed to their lamellar structure, high specific surface area (about 750 $m^2.g^{-1}$) and high aspect ratio [4]. They are basically composed of tetrahedral silica sheets

* Corresponding author.
E-mail address: aurelie.taguet@mines-ales.fr (A. Taguet).

alternating with octahedral alumina sheets in different ratios and are classified into different categories such as (2:1) smectite class including montmorillonite or (1:1) kaolinite class [2,5].

Halloysites nanotubes, HNTs belong to the clay family, more specifically belonging to the (1:1) kaolinite class with an unique tubular structure, consisting of an outer silica tetrahedral surface layer and an inner alumina octahedral surface [2]. Thanks to their tubular structure and high mechanical strength, HNTs are often compared to synthetic nanotubes as carbon nanotubes (CNT) and exhibits numerous other advantages; natural availability, good biocompatibility and low cost. According to Lvov *et al.,* HNT costs around $ 4 per kg against $ 500 per kg for CNT [6]. HNTs are of widespread occurrence in many soils of hydrothermal origin [7,8] and form important natural deposits in China, Japan, New Zealand, Brazil, USA, Turkey, France [9]. The raw material is mined from these natural deposits and easily ground into powder. The HNT molecular formula is $Al_2Si_2O_5(OH)_4.nH_2O$, where n equal 2 and 0, representing hydrated or dehydrated HNT, respectively [8,9]. According to the hydration state, the crystalline structures differ; the freshly mined HNT has a fully hydrated form (n = 2) with an intercalated monolayer of water molecules in the interlayer spaces and the d_{001} spacing is 10 .
The thermal behavior of HNT is characterized by three thermal events [10]: *i)* the dehydratation step with the loss of adsorbed water (surface and interlayer) occurring between 90 °C and 150 °C and the resulting dehydrated HNT forms present a d_{001} spacing at 7 [6,11], *ii)* the dehydroxylation step arises in 450–600 °C range and *iii)* the formation of new phases attributed to amorphous SiO_2 and γ-Al_2O_3. Pure HNTs appear milky white, but according to the deposit origin, different colors from yellow to brown could be observed which could be attributed to the partial substitution of Al or Si by other ions such as Fe, Cr or Ti [12]. As color and purity, the HNT dimensions depend on deposits area. Generally, the HNT length covers a range from submicron scale to several microns, the external diameter range is between 30 and 190 nm and the internal diameter is included between 10 and 100 nm.

Due to the versatile features as a large surface area, a hollow tubular structure and a tailored surface chemistry, HNTs have found numerous applications in many fields as in the drug-controlled release, the nanotemplating and the sorption [9]. Many studies have demonstrated the HNT effective potential as nanocarriers for encapsulation and controlled or sustained release of chemically or biologically active compounds [13–18]. Moreover, the idea to use HNT lumen as nanoreactors or nanotemplates to prepare nanoparticles, nanowires and nanocoatings has been studied [19–21]. Sorption applications of HNTs due to their ability in the adsorption of contaminants and other substances were evaluated which highlighted a novel effective biofilter [22–24]. And mainly, numerous works have been conducted on the HNT addition into polymer matrix to prepare polymer nanocomposites [11,25,26]; in which a consensus on the improvement of materials performances in terms of physical, mechanical and thermal properties has been reported. These works have been carried out in almost all polymer matrices [25]: polyolefins, polyamide, polyester, polystyrene, epoxy resin, polyurethane rubber, *etc*.….

However, very few studies in the literature described the HNT addition into ethylene-co-vinyl acetate, EVA copolymer [27–29]. Bidsorkhi *et al.* [28] prepared EVA nanocomposites filled with 3 wt% of HNT by solvent casting method and demonstrated an improvement of the thermal and mechanical properties of nanocomposites as well as of their ductility, toughness, water resistance and oxygen permeability. Similarly, Padhi *et al.* [27,30] have formulated EVA/HNT nanocomposites with 10 phr loading of unmodified/modified HNT by solvent casting method. In general, the thermal stability and the mechanical properties such as tensile strength, tensile modulus and tear strength of EVA nanocomposites achieved an optimum at 5 phr of unmodified HNT and further decreased due to a poor dispersion and an agglomeration at higher filler loading. In the case of modified HNT (m-HNT) by γ-methacryloxypropyltrimethoxysilane, the intertubular and interfacial interaction of modified HNT and EVA matrix increased and so the agglomeration at higher filler loading was limited which further enhanced the thermal and the mechanical properties of EVA/m-HNT nanocomposites.

EVA copolymer is widely used in various applications, especially in wire and cable industry. The above reported approach to produce EVA/HNT nanocomposites by solvent casting method is not the conventional method to process thermoplastic polymers and it is just not sustainable at the industrial scale. In spite of this observation and an extensive research in literature, the number of studies on EVA/HNT nanocomposites prepared by melt blending process is even lower, almost nonexistent, except the works of Zubkiewicz *et al.* [29,31]. The authors have prepared EVA-based nanocomposites containing from 2 to 8 wt% of HNT by melt blending using a twin screw-extruder. They have shown that with an increasing HNT fillers content up to 8 wt%, the mechanical properties such as the tensile strength and the Young's modulus, the flame retardancy and the thermo-oxidative stability were enhanced. Concerning the interpretations about the thermo-oxidative degradation of EVA and EVA/HNT nanocomposites, the authors emphasized that the thermal degradation was the same for EVA and EVA/HNT nanocomposites that takes place in two steps, each belonging to each part of the copolymer (ethylene and vinyl acetate) [29]. However, if we look closely to the mass loss curves and their derivatives obtained by thermogravimetric analysis, a preliminary degradation step occurs around 250 °C. The authors attributed this mass loss to the evaporation of the physically absorbed water on the HNT surface and some water from interlayer. Nevertheless, the physically absorbed water represents approximately 5% of the HNT mass loss and the HNT content is 8 wt%, thus the mass loss due to physically absorbed water should be barely noticeable, being of 0.4% while the observed mass loss on the curve is about 5% at 250 °C. Hence, as the observed mass loss is more than ten times greater than the corresponding mass loss due to the evaporation of the physically absorbed water, we assume that even if the authors did not mention any thermal degradation of EVA caused by the presence of HNT, there should be one since a brown color appeared in samples during melt blending process [31]. However, to the best of our knowledge, there are no other publications investigating the thermal degradation of EVA/HNT composites. Contrarily, EVA/montmorillonite composites are more often reported in the literature. And the deacetylation of EVA/clays occurring at low temperature is well known in the literature [32–36]. The presence of acid sites on clay surface is renowned for having catalytic effect on the thermal degradation of EVA. Camino *et al.* [32] were the first to describe the preliminary mass loss due to acetic acid release at lower temperature due to the presence of acid sites on the clay surface. Zanetti et al. [37] described a deacetylation of EVA occurring at lower temperature in TGA in the presence of fluorohectorite. Costache *et al.* [36] carried out experiments which consisted to modify the montmorillonite surface with a silane coupling agent in order to protect the acid sites. And so, they have confirmed the hypothesis that the acid sites present at the clays surface have a catalytic effect on the EVA thermal degradation. The HNTs present similar chemical surface and so, the same catalytic effect should be observed. Nevertheless, to the best of our knowledge, there is no quantitative study that has tried to quantify the contribution of the different steps of the thermal degradation of EVA in the presence of HNT. This is the subject of the present paper using a new quantitative method based on TGA/FTIR coupling. Moreover, a correlation with color changes was performed. For this, EVA/HNT composites were produce with different processes (solvent casting or melt blending), different HNT filler contents (up to 30 wt%) and different melt blending temperatures.

2. Experimental

2.1. Material

EVA copolymer with around 28 wt% of vinyl acetate (VA) (EVATANE 28–03), density of 0.93 g.cm^3 and melt flow index of 3–4.5 g/10

min, was supplied by ARKEMA (France). HNTs were purchased from Sigma-Aldrich (Germany). Some informations on commercial HNT are provided in Supporting Information (SI1). These nanotubes had an average tube diameter of 50 nm and an inner lumen diameter of 15 nm with a length around 1–3 μm. Their characteristics were: true density of 2.53 g.cm^3, specific surface area of 64 m^2. g^{-1}, pore volume of 1.26–1.34 mL.g^{-1} and refractive index of 1.54. THF and 3-aminopropyltriethoxysilane (APTS) were supplied by Merck.

2.2. Modified HNT-APTS

3-aminopropyltriethoxysilane (APTS) was grafted onto HNT at a weight ratio of HNT/APTS of 1/0.5 in toluene. The mixture was heated at 120 °C for 24 h. The modified HNT, named HNT-APTS was filtered and washed four times with toluene to remove unreacted APTS. Then, it was dried under vacuum at 100 °C for one night.

2.3. Preparation of EVA/HNT nanocomposites

2.3.1. Nanocomposites produced by melt blending process

EVA/HNT nanocomposites obtained by melt blending process were carried out using an internal mixer, Haake Rheomix 600 (ThermoFischer Scientific) at 50 rpm during 10 min, equipped with a 50 cm^3 tank. The mixing chamber temperature was set at different temperatures from 130 °C up to 190 °C according to the nanocomposite's formulations (Table 1).

2.3.2. Nanocomposites produced by solvent casting method

Some EVA/HNT nanocomposites were performed by solvent casting method. 1.8 g of EVA were dissolved in THF at 50 °C during 1 h and in parallel 0.2 g of HNT were dispersed by sonication in THF in the same conditions. The quantity of dispersed HNT was adapted in function of the final filler content in EVA/HNT nanocomposites (Table 1). The suspension with HNT was added to the EVA solution and was dispersed again by sonication at 50 °C during 1 h, before to be casted over a polyethylene support and dried at room temperature for 1 day.

2.3.3. Nanocomposites films produced by thermocompression

Nanocomposites films (disk of 7 cm in diameter and about 300 μm thick) were obtained as follows. In a first step, nanocomposite compounds were heated during 30 s at 100 °C without pressure between two Teflon-coated plates. Then samples were pressed during 30 s at 100 °C with increasing pressure levels up to 100 bars using a hydraulic forming press (Darragon, 100 T).

Table 1
EVA-based formulations: EVA and EVA/HNT with increased HNT content up to 30 wt% produced by melt blending process (MELT) or by solvent casting method (SOLVENT).

	Formulations	Process conditions		
		wt% EVA	wt% HNT (or wt% HNT-APTS)	Melt temperature (°C)
	Neat EVA	100	/	/
MELT	EVA-130	100	/	130
	EVA/10HNT-130	90	10	130
	EVA-150	100	/	150
	EVA/10HNT-150	90	10	150
	EVA-170	100	/	170
	EVA/10HNT-170	90	10	170
	EVA/20HNT-170	80	20	170
	EVA/30HNT-170	70	30	170
	EVA-190	100	/	190
	EVA/10HNT-190	90	10	190
SOLVENT	EVA-THF	100	/	/
	EVA/10HNT-THF	90	10	/
	EVA/20HNT-THF	80	20	/
	EVA/30HNT-THF	70	30	/
	EVA/30HNT-APTS-THF	70	30	/

2.4. Characterizations of nanocomposites films

2.4.1. Photometry

The color measurements were carried out in a dark room using a CS 1000 spectroradiometer (Konica Minolta). The sample films were superimposed on an opacity chart consisting of black and white areas (BYK). For our study, the measurements were made on the covered white areas. The sample films have been illuminated with a 4700 K light source that approximates CIE D50 daylight (standard corresponding to horizon light) with a smooth, continuous and full spectral power distribution. The color rendering index of the light is 99.35. The measurement geometry has been chosen in order to avoid specular reflexion in the measured area. The measurements of the colorimetric parameters L* , a* and b* indicate color changes; with L* characterizing the lightness from black to white, a* the range of color from green to red, and b* the range color from blue to yellow. Other different deduced parameters consider the color variation; ΔL* as the lightness deviation, Δa* as the deviation on the green-red axis, Δb* as the deviation on the blue-yellow axis and ΔE* as the total color deviation.

$$\Delta L^* = L^*_{sample} - L^*_{neat\ EVA}$$

$$\Delta a^* = a^*_{sample} - a^*_{neat\ EVA}$$

$$\Delta b^* = b^*_{sample} - b^*_{neat\ EVA}$$

$$\Delta E^* = \sqrt{\Delta L^{*2} + \Delta a^{*2} + \Delta b^{*2}}$$

2.4.2. Scanning electron microscopy, SEM

A scanning electron microscope, Quanta 200 ESEM (FEI Company) was used to evaluate the dispersion and distribution states of HNT in EVA copolymer matrix. The SEM micrographs were performed on cryofractured films.

2.4.3. ATR-FTIR

The Fourier Transform Infrared spectroscopy, FTIR analyses of films were performed using a Vertex 70 spectrometer (Bruker) in transmission mode through a "Golden gate" attenuated total reflectance accessory equipped with a diamond crystal. Spectra were obtained from 32 scans with a resolution of 4 cm^{-1} at room temperature in a wavelength range of 4000–400 cm^{-1}.

2.4.4. FTIR-TGA coupling

Thermogravimetric analyses, TGA were carried out using a Setsys Evolution apparatus (Setaram) for samples of 10 ± 2 mg. Each sample were heated at a heating rate of 10 °C/min from room temperature to 900 °C under nitrogen flow of 40 mL/min. The gases released from the pyrolysis were analyzed by Fourier transformed infrared (FTIR) spectroscopy. The gases were sent to the gas cell through a transfer line heated at 200 °C. The FTIR analyses were carried out using a Nicolet iS10 FTIR spectrometer (ThermoFischer Scientific) with a wavelength range of 4000–400 cm^{-1} and a resolution of 2 cm^{-1}.

3. Results and discussion

3.1. Characterization of the HNT-filled EVA nanocomposite films

3.1.1. Macroscopic changes

Visually, pure EVA films appeared transparent and homogeneous regardless of the production method or the melt temperature in melt blending process as shown in Fig. 1. The addition of HNT systematically resulted in a slight opacity and a significant color change of EVA nanocomposite films as well as a release of a strong acetic acid odor. It is

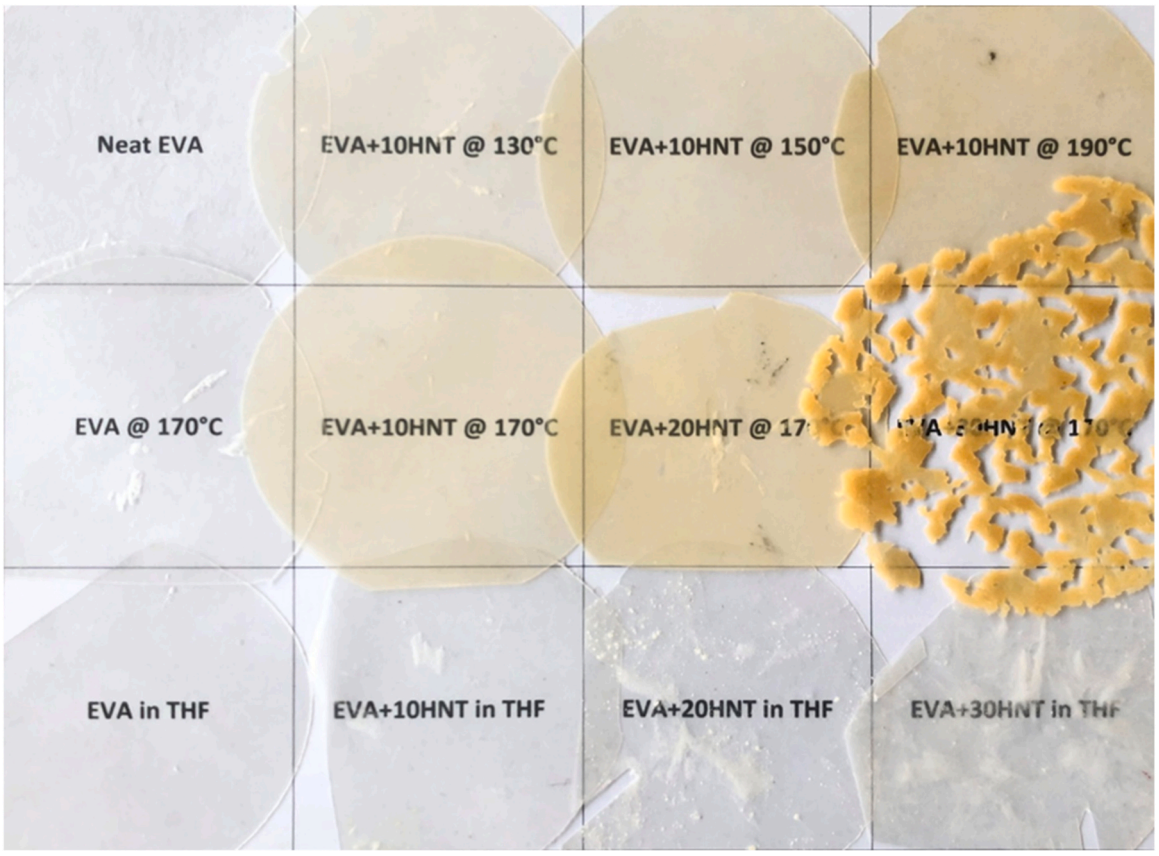

Fig. 1. Photos of EVA-based Films: EVA and EVA/HNT with increased HNT content up to 30 wt% produced by melt blending process (noted "@ 130–190 °C") or by solvent casting method (noted "in THF").

noting the particular issue of EVA+ 30HNT@ 170 °C formulation; the obtention of a homogeneous film could not be achieved. Moreover, the dispersion and distribution of HNT into EVA copolymer matrix by solvent casting method did not enable to obtain a completely homogeneous film, as agglomerates of particles were visually observable. The occurrence of the yellow color was more or less pronounced according to the production method or the melt temperature in melt blending process. Regarding the color changes of EVA/HNT films, several visual observations could be made: *i)* the yellow color was more pronounced in EVA/HNT films obtained by melt blending process by comparison with the solvent casting method, *ii)* a yellow color gradient was observed when the melt temperature in melt blending process was increased, and *iii)* a yellow color gradient was observed when the HNT fillers content was increased.

The color changes of EVA and EVA/HNT films were evaluated by photometry measurements. The visual observations were quantitatively confirmed by the measurements of the colorimetric parameters L* , a* and b* which are reported in Table 2. The films without HNT present similar aspect and close values of L* , b* and a* (grey lines in Table 2). The addition of HNT in EVA copolymer matrix by melt blending process slightly decreased the L* value ($L^*_{EVA+10HNT\ 170\ °C} = 93.3$ vs $L^*_{neat\ EVA} = 97.4$) and significantly increased the b* value ($b^*_{EVA+10HNT\ 170\ °C} = 4.4$ vs $b^*_{neat\ EVA} = -7.7$). This trend was accentuated with an increasing HNT content in EVA copolymer matrix; $b^*_{EVA+10HNT\ 170\ °C} = 4.4$, $b^*_{EVA+20HNT\ 170\ °C} = 15.1$ and $b^*_{EVA+30HNT\ 170\ °C} = 32.3$. However, this trend was much less noticeable when HNT was incorporated in EVA

Table 2
Color parameters expressing the color changes of EVA-based formulations: EVA and EVA/HNT with increased HNT content up to 30 wt% produced by melt blending process or by solvent casting method.

	Formulations	L*	a*	b*	ΔL*	Δa*	Δb*	ΔE*
	Neat EVA	95.4	3.3	-7.7	0	0	0	0
MELT	EVA-130	95.1	3.3	-7.6	-0.2	0	0.1	0.3
	EVA/10HNT-130	93.5	2.3	-1.4	-1.9	-1.0	6.3	6.7
	EVA-150	95.0	3.3	-7.6	-0.4	0	0.1	0.4
	EVA/10HNT-150	94.0	1.7	1.3	-1.4	-1.6	9.0	9.3
	EVA-170	95.1	3.2	-7.4	-0.3	-0.1	0.3	0.4
	EVA/10HNT-170	92.8	1.0	4.4	-2.6	-2.3	12.1	12.5
	EVA/20HNT-170	90.6	0.3	15.1	-4.8	-3.0	22.8	23.5
	EVA/30HNT-170	82.8	3.0	32.3	-12.4	-0.3	40.0	41.9
	EVA-190	95.9	3.3	-7.8	0.5	0	-0.1	0.5
	EVA/10HNT-190	93.1	0.9	6.3	-2.3	-2.4	14.0	14.3
SOLVENT (THF)	EVA	94.6	3.3	-7.5	-0.8	0	0.2	0.8
	EVA/10HNT	96.1	3.0	-6.0	0.7	-0.4	1.7	1.8
	EVA/20HNT	95.8	2.9	-6.1	0.5	-0.4	1.6	1.7
	EVA/30HNT	93.4	2.5	-2.4	-1.9	-0.8	5.2	5.7

copolymer matrix by solvent casting method; if we compare EVA+ 30HNT@ 170 °C and EVA+ 30HNT in THF films, $L^*_{EVA+30HNT\ THF} = 93.4$ was higher than $L^*_{EVA+30HNT\ 170\ °C} = 82.8$ and $b^*_{EVA+30HNT\ THF} = -2.4$ was lower than $b^*_{EVA+30HNT\ 170\ °C} = 32.3$.

3.1.2. Dispersion and distribution of HNT

The HNT dispersion and distribution in EVA matrix were evaluated by SEM observations performed through the whole thickness of the film (Fig. 2). It is clear that higher amounts of HNT in EVA films prepared by solvent casting lead to poorer distribution with the formation of huge aggregates of nanoparticles localized in one part of the thickness of the film. When melt blended by internal mixer, HNT dispersion is better than with solvent casting but it seems that dispersion decreases when the amount of HNT increases.

3.1.3. FTIR spectroscopy

The EVA/HNT nanocomposites films were also characterized by ATR-FTIR spectroscopy and some resulted FTIR spectra are presented in Fig. 3. The characteristic vibrational bands of EVA are observed; both typical bands of vinyl acetate group at: 1736 cm^{-1} (C═O_{ester} stretch), 1236 cm^{-1} (C-O_{ester} antisymmetric stretch), and 1019 cm^{-1} (C-O_{ester} symmetric stretch), and ethylene backbone at: 2917 cm^{-1} (CH_2 antisymmetric stretch), 2849 cm^{-1} (CH_2 symmetric stretch), 1467 cm^{-1} (CH_3 antisymmetric bend), 1371 cm^{-1} (symmetric bend) and 718 cm^{-1} (CH_2 inner rock) are identified [38–40]. The HNT spectrum exhibited characteristic vibrational bands into two wavelength ranges (in grey area on the Fig. 3) [41]. The 3700 – 3600 cm^{-1} range is specific to stretching vibrations of hydroxyl groups (O-H stretch). The vibrational bands at 3694 cm^{-1} and 3622 cm^{-1} are attributed to the stretching vibration of inner surface Al-OH groups. The interlayer H_2O stretching band is observed at 3550 cm^{-1}. There is no characteristic vibrational bands of HNT in the range of 3000 – 1300 cm^{-1}, except a band centered at 1651 cm^{-1} which is ascribed to bending vibrations of H_2O. The vibrational band relating to the stretching bond of Si-O appears at 1003 cm^{-1}. The 1120 cm^{-1} band is assigned to stretching mode of apical Si-O. The vibrational band at 907 cm^{-1} corresponds to bending vibration of inner hydroxyl Al-OH group. HNT spectrum also shows obvious vibrational bands in the 500–400 cm^{-1} range, at 523 cm^{-1} and 461 cm^{-1} due to the deformation of Si-O (Si-O bend) in Al-O-Si and Si-O-Si, respectively.

The EVA degradation induced by the presence of HNT in EVA matrix seems not observable by FTIR analyses in EVA/HNT films. Except a gradual decrease in peak intensities at 1736 and 1236 cm^{-1} and a gradual increase in peak intensities at 1003, 907, 523 and 461 cm^{-1} which are characteristic of vinyl acetate group and Si-O group in HNT, respectively. This observation is in agreement with an HNT content increase in EVA/HNT formulations up to 30 wt% and consequently the vinyl acetate content drop.

3.2. Quantification of the different contributions of the thermal degradation of EVA in presence of HNT

3.2.1. Catalytic effect on thermal degradation of EVA in presence of HNT

In addition to macroscopic/microscopic changes described above, the thermal behavior was studied to highlight changes in EVA thermal degradation in presence of HNT. As previously mentioned, EVA copolymer undergoes two degradation steps: *i)* the first degradation step is due to the release of acetic acid (deacetylation), involving the vinyl acetate units of the polymeric chains and the formation of unsaturated C═C bonds on the backbone (Δm1 = 20% in Fig. 4-a) and *ii)* the second degradation step involves the polyene chain and leads to the complete polymer volatilization, without the formation of a stable residue above 600 °C [32] (Δm2 = 80% in Fig. 4-a). The incorporation of HNT in EVA matrix modifies the thermal degradation pathway. In addition to previous degradation steps, another weight loss appears at a lower temperature around 250 °C as presented in the Fig. 4-a. The DTG curves of EVA/HNT formulations show this new catalytic peak at lower temperature corresponding to acetic acid release, as discussed below (Fig. 4-b).

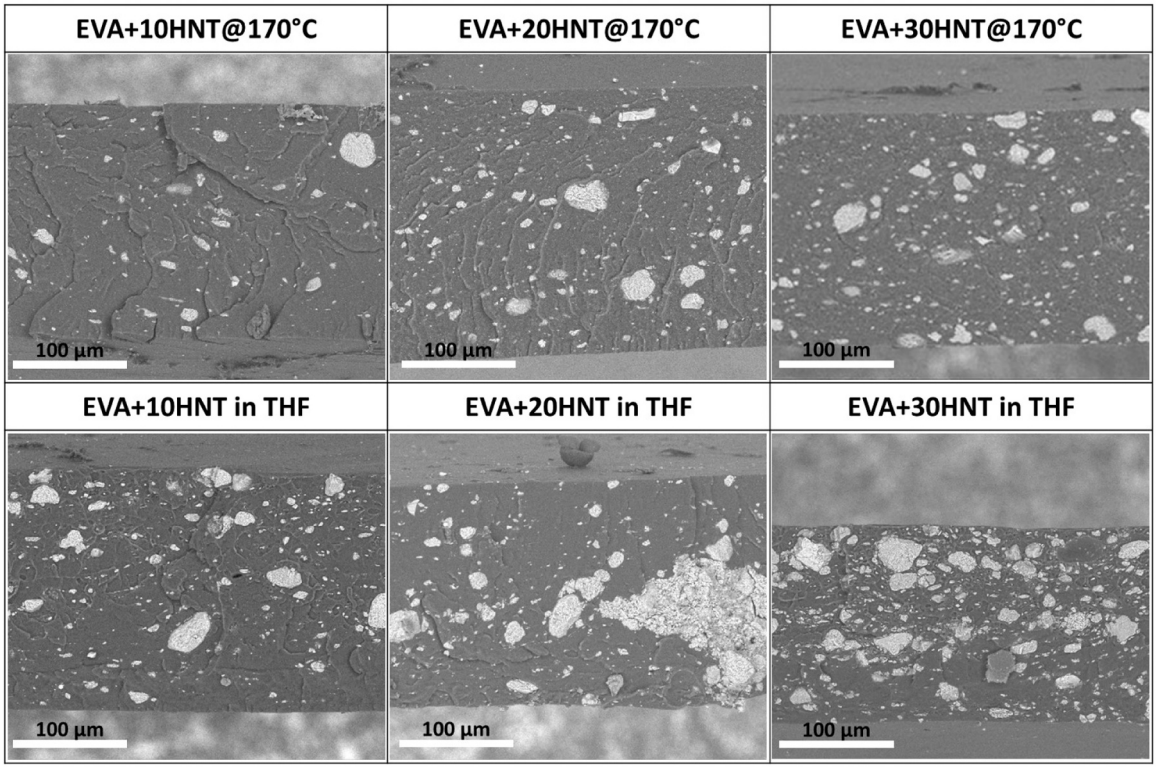

Fig. 2 SEM observations of EVA/HNT films with increased HNT content up to 30 wt% produced by melt blending process at 170 °C and by solvent casting method in THF (Magnification x 400).

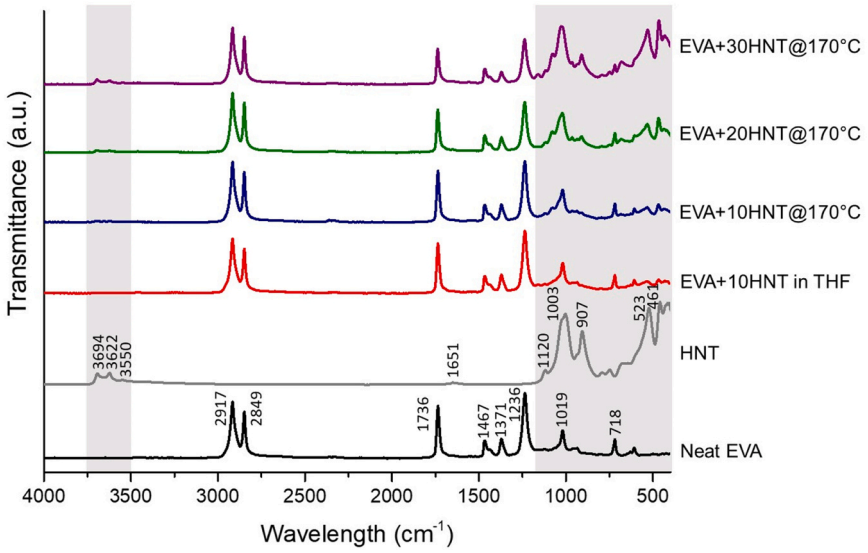

Fig. 3. FTIR spectra of HNT, neat EVA and EVA/HNT films with HNT content up to 30 wt% produced in different conditions.

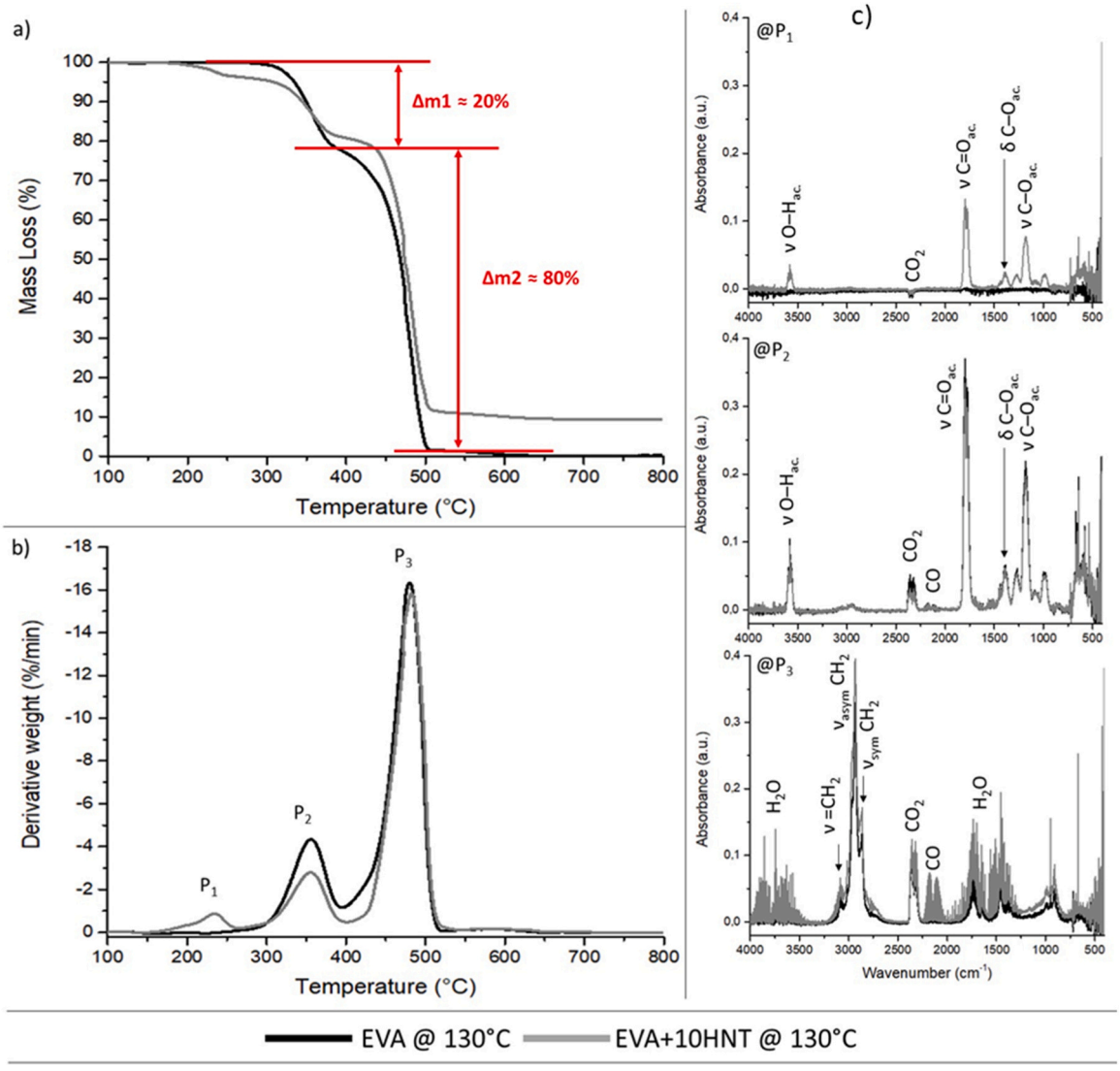

Fig. 4. FTIR-TGA coupling of EVA and EVA+ 10HNT@ 130 °C: a) TG curves and b) DTG curves and c) FTIR gas spectra at P_1, P_2 and P_3.

Moreover, the incorporation of HNT only induces modification of the two first peaks, noted "P_1" for the first acetic acid elimination and "P_2" for the second one, in Fig. 4-b, whereas the peak corresponding to the degradation of the polyene chain is unchanged ("noted P_3"). Moreover, according to the macroscopic observations, and especially the color changing of melt blended EVA/HNT nanocomposites (Table 2), we know that there is a thermal degradation of EVA occurring during the melt blending process and due to the presence of HNT. This phenomenon leads to a fictional degradation peak "noted P_0". Obviously, this P_0 peak cannot be seen by TGA-FTIR as this degradation step has occurred prior to the thermo-analysis of the samples.

In the following section, an approach has been developed based on FTIR-TGA coupling results, in order to quantify the catalytic degradation of EVA due to HNT (namely, P_0 and P_1 steps) and leading to a release of acetic acid at low temperature during the thermal degradation of EVA copolymer.

3.2.2. *Quantification of the different EVA decomposition steps*

Regarding the TG curves of neat EVA copolymer (Fig. 4-a), the released acetic acid represents a weight loss around 20 wt%. This weight loss represents 70% of the nominal vinyl acetate (VA) content which is 26–28 wt% for the studied EVA copolymer grade. This difference between the evolved acetic acid and the nominal VA values corresponds to the ratio between the molecular masses of acetic acid (CH_3COOH) and vinyl acetate ($CH_3COOC_2H_3$) (Eq. 1) [42].

$$Ratio = \frac{M_{CH_3COOH}}{M_{CH_3COOC_2H_3}} = \frac{60.05}{86.09} = 70\% \quad (1)$$

As previously mentioned, usually EVA copolymer degradation occurs into two steps: *i)* the current (or regular) released acetic acid gas corresponds to the first peak at 350 °C, noted "P_2" and *ii)* the degradation of the polyethylene part of the copolymer corresponds to the second peak around 500 °C, noted "P_3". The presence of HNT induced a catalytic effect with the occurrence of a peak at 250 °C, noted "P_1". The released gases during the thermal degradation in TG analysis are identified by FTIR from the P_1, P_2 and P_3 peaks in DTG curves and are presented in Fig. 4-c. The FTIR spectrum from P_2 corresponds mainly to acetic acid which is confirmed by the presence of characteristic bands at: 3582 cm^{-1} (O-H_{ac}. stretch), 1795 cm^{-1} (C=O_{ac}. stretch), 1387 cm^{-1} (O-H_{ac}. bend) and 1186 cm^{-1} (C-O_{ac}. stretch). Moreover, small amounts of CO_2 (around 2350 cm^{-1}) and CO (around 2150 cm^{-1}) are detected which discloses a secondary partial acetate decomposition into CO, CO_2, ketene and water as reported in the literature [32,43,44]. This reaction of deacetylation should lead to the formation of unsaturated C=C bonds in polymer backbone, as demonstrated in the literature [45,46]. At P_3, the degradation of the polymeric chain corresponds to a complex hydrocarbon mixture including alkanes, alkenes and small aromatic compounds [32]. The FTIR spectrum acquired at P_3 is in accordance with the literature [32,36,47,48], and presents the characteristic bands at: 3019 cm^{-1} (=CH_2 stretch), 2934 cm^{-1} (-CH_2- asymmetrical stretch), and 2865 cm^{-1} (-CH_2- symmetrical stretch). Moreover, in presence of HNT, the presence of water is detected (numerous bands around 3800 cm^{-1} and 1600 cm^{-1}) which corresponds to the dehydroxylation of HNT operating at 450 °C [10]. Despite being under nitrogen flux, characteristic bands of CO_2 (around 2350 cm^{-1}) and CO (around 2150 cm^{-1}) are observed which may be explained by a limited nitrogen flux (only 40 mL/min) or by the presence of condensed species due to previous degradation steps.

The FTIR spectra obtained for P_2 and P_3 for EVA@ 130 °C and EVA+ 10HNT@ 130 °C, both prepared by melt blending (Fig. 4-c) showed no significant differences; same characteristic vibrational bands are observed and their intensity variation are not noticeable. The obvious difference concerns the FTIR spectra at P_1. There is no vibrational band all over the FTIR spectrum for EVA@ 130 °C, indicating no degradation before 250 °C. For EVA+ 10HNT@ 130 °C, vibrational bands are observed on the FTIR spectrum and they are characteristic of acetic acid, as for FTIR spectra at P_2. The only difference between spectra from P_1 and P_2 is the intensity of vibrational bands; the absorbance of C=O_{ac} stretching band is around 0.4 arbitrary unit (a.u.) for P_2 and it is less than 0.2 a.u. for P_1.

In order to quantify the fractions of released gases, a new method is developed, based on the hypothesis of the presence of three CH_3COOH gas populations. Previously, it has been demonstrated for melt blended HNT-filled EVA formulations that TG analysis showed the presence of two peaks assigned to acetic acid elimination; i.e. a catalytic CH_3COOH gas population (P_1 on DTG curves) and the "regular" CH_3COOH gas population (P_2 on DTG curves). These two CH_3COOH gas populations are observed on DTG curves and also by FTIR analysis. The area of the vibrational band C=$O_{ac.}$ at 1795 cm^{-1} is monitored and a Gram-Schmidt curve is plotted, based on the vector analysis and the reconstruction of acquired interferograms which allows to plot the total evolved CH_3COOH gas detected by the spectrometer. Fig. 5 presents the Gram-Schmidt curves for evolved CH_3COOH gas normalized to the EVA mass for each sample. As DTG curves, the Gram-Schmidt curves present two peaks of acetic acid gas corresponding to P_1 and P_2. For EVA+ 10HNT@ 130 °C, the P_1 intensity is about 0.37 a.u./mg whereas it is only about 0.18 a.u./mg for EVA+ 10HNT@ 170 °C. Hence, the P_1 intensity decreases from EVA+ 10HNT@ 130 °C to EVA+ 10HNT@ 170 °C and has disappeared for EVA+ 10HNT@ 190 °C and EVA+ 30HNT@ 170 °C.

However, as mentioned previously, another CH_3COOH gas population corresponds to the release of acetic acid during processing (named "P_0" peak), i.e. before TG analysis. This release of acetic acid is confirmed by the released strong acetic acid odor after melt blending process. The strong acetic acid odor was undetected for neat EVA or EVA-HNT samples obtained by solvent casting method. A quantitative method by iterative approach is proposed and it is based on the hypothesis that the three CH_3COOH gas populations, counting for 20 wt% of EVA total mass, are: *i)* a CH_3COOH fraction released during the melting blend process (assigned to P_0), *ii)* a CH_3COOH released at low temperature under TGA (assigned to P_1); both fractions are related to the catalytic action of HNT, and *iii)* a "regular" CH_3COOH fraction released in TGA at around 350 °C (assigned to P_2) as observed for neat EVA.

The peak area measurements on Gram-Schmidt curves are assigned to CH_3COOH gas normalized to the EVA mass in sample and are respectively named A_1 and A_2 (corresponding to P_1 and P_2) in the following text. The peak area of CH_3COOH gas population corresponding to the release of acetic acid during melt blending process is named A_0

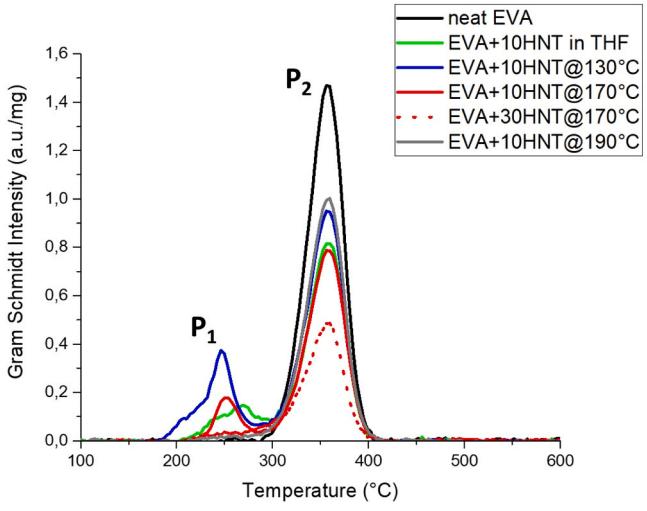

Fig. 5. Gram Schmidt curves of released CH_3COOH gas in TG analysis for neat EVA and different EVA-based formulations. The Gram Schmidt intensity was normalized considering the mass of EVA for each formulation.

and it is calculated as following (Eq. 2):

$$A_0 = 100 * \frac{A_{ref} - (A_1 + A_2)}{A_{ref}} \quad (2)$$

where A_{ref} corresponds to the peak area (in %) for neat EVA.

The sum of $A_0 + A_1$ corresponds to the catalytic released gas due to the presence of HNT and the sum of the three acetic acid fractions, $A_0 + A_1 + A_2$ represents a weight loss around 20 wt%. for each sample. It is important to emphasize that due to the release of acetic acid during processing, the composition of the samples analyzed under TGA is not exactly the initial one. Indeed, the samples are slightly poorer in EVA, especially in vinyl acetate, and richer in HNT than expected. The initial mass of the sample (before TGA measurement) has to be adjusted to take into account this weight loss during processing step. First, the maximum area of the vibrational band C=$O_{ac.}$ at 1795 cm^{-1} is calculated using neat EVA and named A_{ref}. A_1 and A_2 are measured (per g of EVA) and compared to the maximum area, A_{ref}. The fraction A_0 is estimated as the difference between the VA content and the sum of A_1 and A_2. This value is slightly overestimated due to the error on the EVA content in the sample. Then, considering this fraction, the sample composition is re-calculated and the calculations are carried out once again. Several iterations are needed to obtain a stable sample composition; i.e. a composition which does not change anymore after a further iteration (see Supporting Information, SI2). The final results are summarized in the Table 3.

3.3. *Influence of different parameters on the EVA thermal degradation*

3.3.1. *Determination of catalytic effect*

As already stated, the addition of HNT into EVA copolymer matrix induces a more or less important catalytic effect on the EVA thermal degradation pathway. This effect has been quantified using the iterative approach described above. In this study, different parameters have been evaluated: *i)* the nanocomposites production method (melt blending process or solvent casting method), *ii)* the different HNT contents for each process, and *iii)* the different melting temperatures for the melt blending process.

Fig. 6 represents the three different fractions; A_0, A_1 and A_2 of the released acetic acid gas for EVA+ 10HNT nanocomposites obtained by solvent casting method (circle signs in green boxes in Fig. 6) or by melt blending process at different processing temperatures (triangle signs in Fig. 6). Concerning the CH_3COOH fraction released at around 350 °C, A_2, (grey signs in Fig. 6) it is relatively stable around 80% whatever the nanocomposite production method or the melt blending temperature. Even if the 80/20 proportion assigned to A_2 versus $A_0 + A_1$ is difficult to explain, we can assume that it is linked to the dispersion of HNT into the

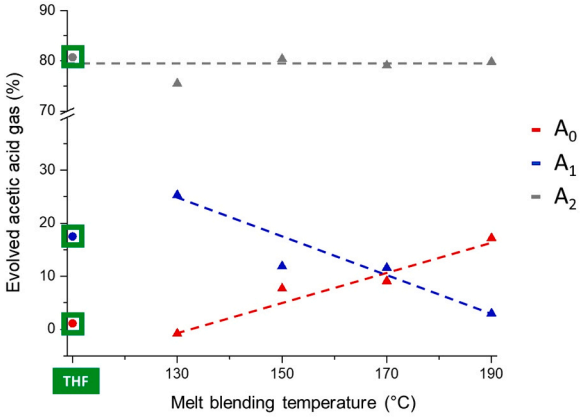

Fig. 6. Graphical representation of the distribution of the evolved acetic acid gas between A_o, A_1 and A_2 for EVA+ 10HNT nanocomposites obtained by different processing methods (solvent casting method with circle signs • in green boxes and melt blending process with triangle signs ▲) and for different melt blending temperatures. The dotted lines are drawn as eyes guideline.

EVA matrix and the possible interaction between the HNT surface and VA part of the EVA chains. The two fractions of released acetic acid for EVA+ 10HNT nanocomposites. A_0 (the CH_3COOH fraction released during the melting blend process) and A_1 (the CH_3COOH fraction released at 250 °C), correspond to the catalytic released acetic acid. In the case of solvent casting, A_0 is negligible and A_1 represents around 20% of the total acetic acid. In the case of melt blending, A_0 is no longer negligible. The sum of A_0 and A_1 is rather constant (around 20%) but the proportions of both fractions change according to the processing conditions. At low melt blending temperature, A_1 fraction is predominant, hence few catalytic CH_3COOH is released during the process. A_1 value decreases when the melt blending temperature increases whereas the A_0 value increases in the same time. At higher melt blending temperatures, A_0 fraction becomes predominant and few catalytic CH_3COOH is released during TGA. For EVA+ 10HNT performed at 190 °C, the available catalytic CH_3COOH is almost fully released during the process (A_1 value is almost negligible). Noting that A_0 value is not zero for formulations obtained by solvent casting method while there is no decomposition expected during processing according the absence of macroscopic changes (no strong odor of acetic acid and no color change). This non-zero value is attributed to uncertainties of measurement in the FTIR-TGA coupling.

Fig. 7 demonstrates the influence of HNT content in EVA-based nanocomposites on the evolved acetic acid gas by comparing the processing methods (solvent casting method or melt blending process at

Table 3
Determination of the different evolved acetic acid gas fractions (A_0, A_1 and A_2) by FTIR-TGA coupling and iterative approach. It must be noticed that for EVA formulations without HNT and so without catalytic effect, A_0 and A_1 are close to zero.

	Formulations	A_1 measured	A_2 measured	$A_1 + A_2$ measured	A_0 (%)	A_1 (%)	A_2 (%)	$A_0 + A_1 + A_2$ (%)
	Neat EVA	0	54.5	54.5	0	0	100	100
MELT	EVA-130	0	55.1	55.1	-0.9	0	100,9	100
	EVA/10HNT-130	13.8	41.2	55.0	-0.8	25.3	75.5	100
	EVA-150	0	54.5	54.5	0	0	100	100
	EVA/10HNT-150	6.4	43.1	49.5	7.7	11.9	80.4	100
	EVA-170	0	53.6	53.6	1.3	0	98.7	100
	EVA/10HNT-170	6.2	42.4	48.7	9.1	11.6	79.1	99.8
	EVA/20HNT-170	1.2	37.6	38.9	24.9	2.3	72.6	99.8
	EVA/30HNT-170	1.5	28.7	30.3	39.6	3.0	57.2	99.8
	EVA-190	0	53.9	53.9	0.9	0	99.1	100
	EVA/10HNT-190	1.6	42	43.6	17.2	3.0	79.8	100
SOLVENT (THF)	EVA	0	53.3	53.3	1.8	0	98.2	100
	EVA/10HNT	9.5	43.9	53.8	1.1	17.5	80.7	99.3
	EVA/20HNT	10.5	42	52.5	3.1	19.4	77.5	100
	EVA/30HNT	12.5	42.9	55.4	-1.4	22.9	78.5	100

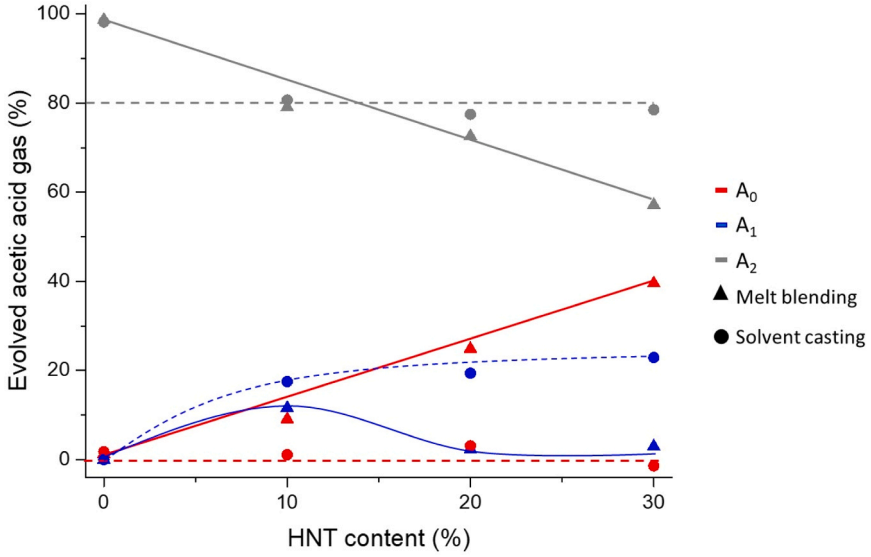

Fig. 7. Graphical representation of the distribution of the evolved acetic acid gas according to the HNT content in nanocomposites, by comparing the processing methods: solvent casting method with circle signs ● and dotted line and melt blending process performed at 170 °C with triangle signs ▲ and solid line). The drawn lines are plotted as eyes guideline.

170 °C). For neat EVA, A_2 is equal to 100% which evidences that in the absence of HNT there is no catalytic effect whatever the production process. For EVA+HNT nanocomposites, concerning A_2 (the CH_3COOH fraction released at around 350 °C), two trends are clearly observed depending on the processing. For solvent casting method, as previously mentioned, A_2 values are relatively stable around 80%. This implies that between 10 and 30 wt% of HNT in EVA, the fractions of acetic acid released through a catalytic process ($A_0 + A_1$) are constant at about 20 wt%, whatever the HNT content. This is not the same case for melt blending process: the A_2 values decrease when the HNT content increases into EVA copolymer matrix; A_2 values decrease from 100% to 57% from 0 to 30 wt% of HNT. This is consistent with our previous argument saying that the dispersion of HNT into the EVA matrix and the possible interaction between the HNT surface and VA part of EVA plays a key role in the catalytic degradation of EVA before 350 °C (corresponding to $A_0 + A_1$). Indeed, as shown in Fig. 2, the dispersion of 30 wt % HNT is better when the sample is prepared by melt blending than by solvent casting. Hence, as there are more interactions between HNT nanotubes and VA part of EVA in EVA+ 30HNT@ 170 °C than in EVA+ 30HNT in THF, the catalytic effect ($A_0 + A_1$) is higher (43%) for EVA+ 30HNT@ 170 °C than for in EVA+ 30HNT in THF (20%).

The A_0 values describe two different trends depending on the nanocomposites production method; *i)* for solvent casting method, no acetic acid is released during process (A_0 value is close to zero represented by red dotted line on Fig. 7) whereas *ii)* for melt blending process, A_0 value increases when HNT content increases. These two different behaviors could be correlated to the macroscopic changes; there are no strong odor of acetic acid and no color change for nanocomposites obtained by solvent casting method in contrast to the nanocomposites obtained by melt blending process as shown in Table 2. The A_1 values seem to be roughly stable for solvent casting method and reach a plateau around 20% at 10 wt% of HNT content (blue dotted line on Fig. 7). The A_1 values obtained by melt blending process start to increase before to decrease (while A_0 increases); it would appear that a maximum value is reached at about 11.5% for 10 wt% of HNT content, before to decrease around 2%.

3.3.2. *Correlation with color deviations*

As presented above, the color changes of nanocomposite films are evaluated by the measurements of the colorimetric parameters L* , a* and b* in the CIELAB system and different parameters considering the color variation (Table 2). Regarding these results, few variations on the green-red axis are noticeable and they are more slightly pronounced on the lightness axis. The major variations occur on the blue-yellow axis which implies a significant increase of ΔE* , as the total color deviation. According to these observations, Fig. 8 shows the relationship between parameters deduced from FTIR-TGA coupling (fraction of acetic acid released during processing, A_0) and color measurements due to the thermal degradation of EVA. A proportional linear trend seems to be emerging especially for EVA+HNT films obtained by melt blending process (red triangle signs on Fig. 8-a). When ΔE* values and A_0 percentages are close to zero (i.e., $\Delta E^* < 2$ and $A_0 < 3\%$), the experimental points for all films without HNT (black square, blue triangle and blue circle signs on Fig. 8-b) are grouped around zero. In the grouped area, we also observe the representative points of EVA+HNT films obtained by solvent casting method (red circle signs on Fig. 8-b). This means that there are not much color changing and catalytic degradation of EVA when the process used is solvent casting (even with HNT) or when EVA is melt processed without HNT (even at high temperature). Nevertheless, a slight ΔE* variation ($\Delta E^* > 5$) for EVA+ 30HNT in THF could be explained by poor dispersion and distribution of HNT into EVA matrix, through solvent casting method at high HNT content (at 30 wt%). The Fig. 8 allows to demonstrate a correlation between the film color changes of the melt blended samples and the catalytic degradation of HNT during the process.

3.4. *Catalytic protection approach*

In order to avoid the catalytic effect induced by HNT on the EVA thermal degradation, HNT was modified with 3-aminopropyltriethoxysilane (APTS) in non-anhydrous condition and silanes can self-condense as shown in SI3 (supporting information) and as demonstrated by Sahnoune et al. [49]. Fig. 9 shows the thermal gravimetric analysis of EVA compared to EVA+HNT and EVA+HNT-APTS. The evolution of mass versus temperature (Fig. 9a) clearly shows a prior degradation of EVA for the EVA+HNT sample which is due to the catalytic effect of pure HNT (as demonstrated before). This is identified by a DTG peak centered at 240 °C, equivalent to P_1 peak. This catalytic effect shown with HNT is cancelled when HNT is grafted with 2 wt% of APTS (SI4). Indeed, there is no degradation for EVA+HNT-APTS centered at 240 °C (absence of P_1 peak for EVA+HNT-APTS in Fig. 9b). Regarding the P_2 peak on Fig. 9b, the ones of EVA and EVA+HNT-APTS are almost

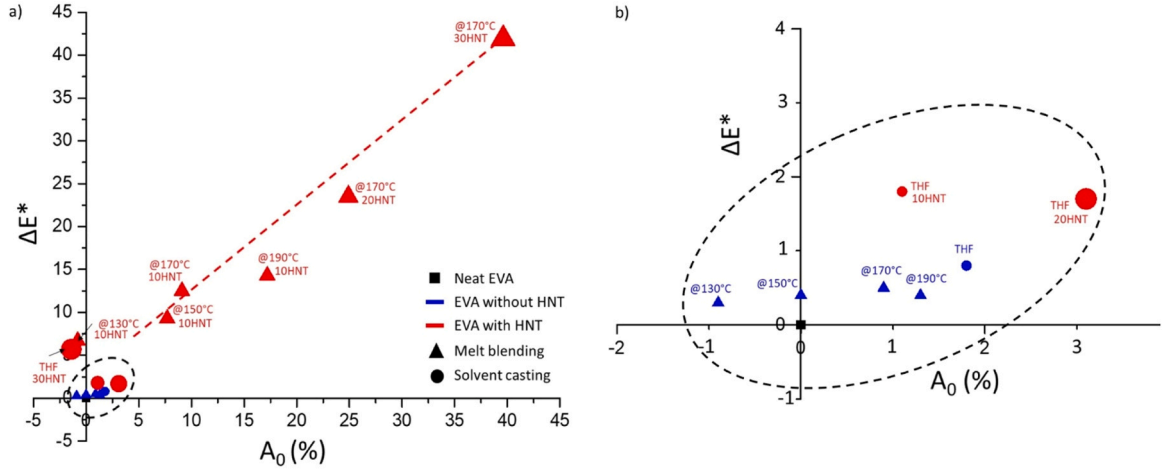

Fig. 8. Graphical representation of $\Delta E^* = f(A_0)$ for EVA-based films: EVA and EVA/HNT with increased HNT content up to 30 wt% produced by melt blending process or by solvent casting method (a) Overall representation and b) Focus representation at lower values of ΔE^* and A_0. Increasing size of the triangles and circles signs represent increasing amounts of HNT. The drawn line/group are as eyes guideline.

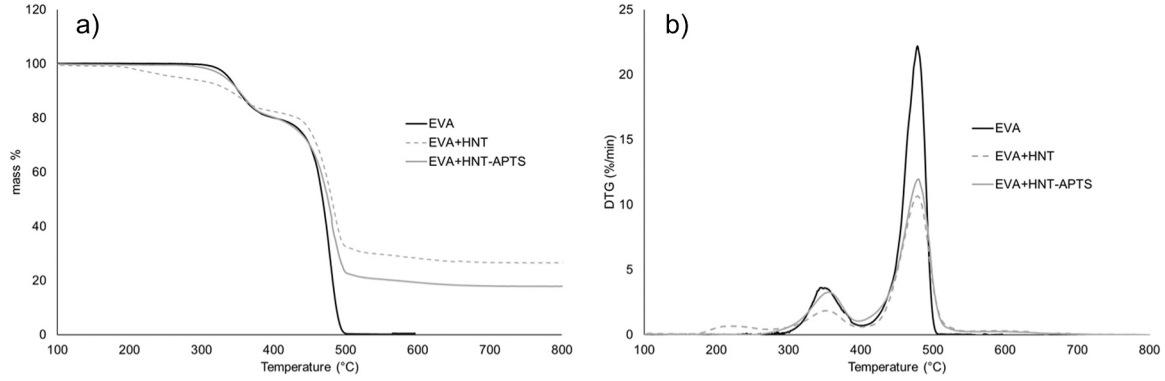

Fig. 9. TGA analysis of EVA, EVA with unmodified HNT and EVA with HNT modified with APTS. a): mass versus temperature; b): DTG versus temperature.

equivalent (same area of P_2 peak) whereas that of EVA+HNT is much lower due to the prior thermal degradation of vinyl acetate catalyzed by pure HNT for this sample.

Due to the non anhydrous conditions for the reaction of APTS onto HNT, it is probable that APTS has self-condensed, leading to grafting rate of 2 wt% (see SI3 and SI4). Hence, the protective effect of APTS can be due to the fact that the silane forms a coating around the nanoclay (see SI3) and hinder the hydroxyl groups at the inner and outer surface of halloysite to catalyze the EVA degradation and start to form acetic acid at 200 °C under TGA.

4. Conclusions

The present article has used TGA combined to FTIR to separate and quantify the different phases of thermal degradation of EVA in the presence of halloysite nanotubes. It is seen that among the four contributions of thermal degradation (from A_0 to A_3 assigned to P_0 to P_3 peaks in TGA, respectively), three are attributed to the degradation of the VA part of EVA copolymer (A_0, A_1 and A_2), among which A_0 and A_1 correspond to catalytic effects due to the presence of HNT. A_0 represents the thermal degradation contribution catalyzed under melt process, whereas A_1 is catalyzed at 250 °C in TGA. An iterative method is used to estimate the contribution of each contribution of the VA degradation and it is seen that when the EVA+HNT films are prepared by solvent casting, the contribution of A_0, A_1 and A_2 are 0%, 20% and 80%, respectively, whatever the HNT content. This constant value of A_2 is probably due to a poor dispersion and distribution of HNT with solvent casting process. However, when EVA+ 10HNT films are prepared by melt blending process, increasing the process temperature leads to an increase in the A_0 contribution while keeping $A_0 + A_1 = 20\%$ (and $A_2 = 80\%$). Finally, the influence of the HNT content in the case of melt processing is significant as A_0 reaches 40% ($A_1 = 2\%$ and $A_2 = 58\%$) with 30% of HNT and a processing temperature at 170 °C. These values obtained for EVA+ 30HNT @ 170 °C mean that 40% of the VA is degraded during processing. The better dispersion of HNT into EVA with melt processing (regarding to solvent process) increases the surface area of contact between HNT and EVA that increases the catalytic degradation of EVA. This catalytic degradation can be avoided by grafting an organosilane (APTS) on the nanotubes that forms a coating around the nanoparticles. Finally, a quantitative correlation was made between the catalytic degradation during the melt process (A_0 contribution) and the color changing. This last result opens perspectives on the possibility of establishing calibration curves based on colorimetry studies to quantitatively assess the thermal degradation of composites.

Funding

This work was provided by the HAREDY project, " HAlloysite nanotubes as flame REtardant carrier in PE/EVA blends for innovative formulations for wire and cable inDustrY ", which is supported by ANR (Agence Nationale de la Recherche) through the contract No ANR-18-CE06–0020.

Declaration of Competing Interest

The authors declare the following financial interests/personal relationships which may be considered as potential competing interests: Aurelie Taguet reports financial support was provided by French National Research Agency.

Data Availability

Data will be made available on request.

Appendix A. Supporting information

Supplementary data associated with this article can be found in the online version at doi:10.1016/j.jaap.2023.106276.

References

[1] J. Jordan, K.I. Jacob, R. Tannenbaum, M.A. Sharaf, I. Jasiuk, Experimental trends in polymer nanocomposites—a review, Mater. Sci. Eng.: A vol. 393 (1–2) (2005) 1–11, https://doi.org/10.1016/j.msea.2004.09.044.

[2] A. Dantas de Oliveira, C. Augusto Gonçalves Beatrice, Polymer Nanocomposites with Different Types of Nanofiller. in Nanocomposites - Recent Evolutions, IntechOpen, 2019, https://doi.org/10.5772/intechopen.81329.

[3] S. Sinha Ray, M. Okamoto, Polymer/layered silicate nanocomposites: a review from preparation to processing, Prog. Polym. Sci. vol. 28 (11) (2003) 1539–1641, https://doi.org/10.1016/j.progpolymsci.2003.08.002.

[4] N. Bitinis, M. Hernandez, R. Verdejo, J.M. Kenny, M.A. Lopez-Manchado, Recent Advances in Clay/Polymer Nanocomposites, Adv. Mater. vol. 23 (44) (2011) 5229–5236, https://doi.org/10.1002/adma.201101948.

[5] M. Kotal, A.K. Bhowmick, Polymer nanocomposites from modified clays: Recent advances and challenges, Prog. Polym. Sci. vol. 51 (2015) 127–187, https://doi.org/10.1016/j.progpolymsci.2015.10.001.

[6] Y.M. Lvov, D.G. Shchukin, H. Möhwald, R.R. Price, Halloysite clay nanotubes for controlled release of protective agents, ACS Nano vol. 2 (5) (2008) 814–820, https://doi.org/10.1021/nn800259q.

[7] S. Hillier, et al., Correlations among the mineralogical and physical properties of halloysite nanotubes (HNTs), Clay Min. vol. 51 (3) (2016) 325–350, https://doi.org/10.1180/claymin.2016.051.3.11.

[8] E. Joussein, S. Petit, J. Churchman, B. Theng, D. Righi, B. Delvaux, Halloysite clay minerals — a review, Clay Min. vol. 40 (4) (2005) 383–426, https://doi.org/10.1180/0009855054040180.

[9] M. Du, B. Guo, D. Jia, Newly emerging applications of halloysite nanotubes: a review, Polym. Int. vol. 59 (5) (2010) 574–582, https://doi.org/10.1002/pi.2754.

[10] K. Belkassa, F. Bessaha, K. Marouf-Khelifa, I. Batonneau-Gener, J. dominique Comparot, A. Khelifa, Physicochemical and adsorptive properties of a heat-treated and acid-leached Algerian halloysite, Colloids Surf. A Physicochem Eng. Asp. vol. 421 (2013) 26–33, https://doi.org/10.1016/j.colsurfa.2012.12.048.

[11] M. Liu, Z. Jia, D. Jia, and C. Zhou, Recent advance in research on halloysite nanotubes-polymer nanocomposite, Progress in Polymer Science, vol. 39, no. 8. Elsevier Ltd, pp. 1498–1525, 2014. doi: 10.1016/j.progpolymsci.2014.04.004.

[12] W. Ma, H. Wu, Y. Higaki, A. Takahara, Halloysite nanotubes: green nanomaterial for functional organic-inorganic nanohybrids (John Wiley and Sons Inc), Chem. Rec. vol. 18 (7) (2018) 986–999, https://doi.org/10.1002/tcr.201700093.

[13] M. Massaro, et al., Chemical modification of halloysite nanotubes for controlled loading and release (Royal Society of Chemistry), J. Mater. Chem. B vol. 6 (21) (2018) 3415–3433, https://doi.org/10.1039/c8tb00543e.

[14] Y. Lvov, W. Wang, L. Zhang, R. Fakhrullin, Halloysite Clay Nanotubes for Loading and Sustained Release of Functional Compounds, Adv. Mater. vol. 28 (6) (2016) 1227–1250, https://doi.org/10.1002/adma.201502341.

[15] N.G. VEERABADRAN, R.R. PRICE, Y.M. LVOV, Clay nanotubes for encapsulation and sustained release of drugs, Nano vol. 02 (02) (2007) 115–120, https://doi.org/10.1142/S1793292007000441.

[16] S.R. Levis, P.B. Deasy, Characterisation of halloysite for use as a microtubular drug delivery system, [Online]. Available.: www. elsevier. Com. /locate/ijpharm (2002).

[17] M. Massaro, et al., Halloysite nanotubes for efficient loading, stabilization and controlled release of insulin, J. Colloid Interface Sci. vol. 524 (2018) 156–164, https://doi.org/10.1016/j.jcis.2018.04.025.

[18] E. Abdullayev, R. Price, D. Shchukin, Y. Lvov, Halloysite tubes as nanocontainers for anticorrosion coating with benzotriazole, ACS Appl. Mater. Interfaces vol. 1 (7) (2009) 1437–1443, https://doi.org/10.1021/am9002028.

[19] G. Liu, F. Kang, B. Li, Z. Huang, X. Chuan, Characterization of the porous carbon prepared by using halloysite as template and its application to EDLC, J. Phys. Chem. Solids vol. 67 (5–6) (2006) 1186–1189, https://doi.org/10.1016/j.jpcs.2006.01.044.

[20] A. Kumar, S.S. Han, Enhanced mechanical, biomineralization, and cellular response of nanocomposite hydrogels by bioactive glass and halloysite nanotubes for bone tissue regeneration, Mater. Sci. Eng. C. vol. 128 (2021), https://doi.org/10.1016/j.msec.2021.112236.

[21] Y. Fu, L. Zhang, Simultaneous deposition of Ni nanoparticles and wires on a tubular halloysite template: A novel metallized ceramic microstructure, J. Solid State Chem. vol. 178 (11) (2005) 3595–3600, https://doi.org/10.1016/j.jssc.2005.09.022.

[22] M. Zhao, P. Liu, Adsorption behavior of methylene blue on halloysite nanotubes, Microporous Mesoporous Mater. vol. 112 (1–3) (2008) 419–424, https://doi.org/10.1016/j.micromeso.2007.10.018.

[23] A. Kilislioglu, B. Bilgin, Adsorption of uranium on halloysite, " Oldenbourg Wiss. (2002).

[24] L. Tymczyna, A. Chmielowiec-Korzeniowska, A. Drabik, The effectiveness of various biofiltration substrates in removing bacteria, endotoxins, and dust from ventilation system exhaust from a chicken hatchery, Poult. Sci. vol. 86 (10) (2007) 2095–2100, https://doi.org/10.1093/ps/86.10.2095.

[25] A. Kausar, Review on Polymer/Halloysite Nanotube Nanocomposite, Polymer - Plastics Technology and Engineering, vol. 57, no. 6. Taylor and Francis Inc., pp. 548–564, Apr. 13, 2018. doi: 10.1080/03602559.2017.1329436.

[26] C.I. Idumah, A. Hassan, J. Ogbu, J.U. Ndem, and I.C. Nwuzor, Recently emerging advancements in halloysite nanotubes polymer nanocomposites, Composite Interfaces, vol. 26, no. 9. Taylor and Francis Ltd., pp. 751–824, Sep. 02, 2019. doi: 10.1080/09276440.2018.1534475.

[27] S. Padhi, P.G.R. Achary, N.C. Nayak, Mechanical and morphological properties of modified halloysite nanotube filled ethylene-vinyl acetate copolymer nanocomposites, J. Polym. Eng. vol. 38 (3) (2018) 271–279, https://doi.org/10.1515/polyeng-2017-0075.

[28] H.C. Bidsorkhi, H. Adelnia, R. Heidar Pour, M. Soheilmoghaddam, Preparation and characterization of ethylene-vinyl acetate/halloysite nanotube nanocomposites, J. Mater. Sci. vol. 50 (8) (2015) 3237–3245, https://doi.org/10.1007/s10853-015-8891-6.

[29] A. Zubkiewicz, A. Szymczyk, S. Paszkiewicz, R. Jędrzejewski, E. Piesowicz, J. Siemiński, Ethylene vinyl acetate copolymer/halloysite nanotubes nanocomposites with enhanced mechanical and thermal properties, J. Appl. Polym. Sci. vol. 137 (38) (2020), https://doi.org/10.1002/app.49135.

[30] S. Padhi, P. Ganga, R. Achary, and N.C. Nayak, Mechanical and morphological properties of halloysite nanotubes filled ethylene-vinyl acetate copolymer nanocomposites, 2017.

[31] A. Zubkiewicz, A. Szymczyk, P. Franciszczak, A. Kochmanska, I. Janowska, S. Paszkiewicz, Comparing multi-walled carbon nanotubes and halloysite nanotubes as reinforcements in EVA nanocomposites, Materials vol. 13 (17) (2020), https://doi.org/10.3390/MA13173809.

[32] G. Camino, R. Sgobbi, A. Zaopo, S. Colombier, C. Scelza, Investigation of flame retardancy in EVA,", Fire Mater. vol. 24 (2) (2000) 85–90, https://doi.org/10.1002/1099-1018(200003/04)24:2<85::AID-FAM724>3.0.CO;2-T.

[33] M. Zanetti, G. Camino, R. Thomann, R. Mülhaupt, Synthesis and thermal behaviour of layered silicate–EVA nanocomposites, Polym. (Guildf.) vol. 42 (10) (2001) 4501–4507, https://doi.org/10.1016/S0032-3861(00)00775-8.

[34] A. Riva, M. Zanetti, M. Braglia, G. Camino, L. Falqui, Thermal degradation and rheological behaviour of EVA/montmorillonite nanocomposites, Polym. Degrad. Stab. vol. 77 (2) (2002) 299–304, https://doi.org/10.1016/S0141-3910(02)00065-4.

[35] M. Batistella, B. Otazaghine, R. Sonnier, A.S. Caro-Bretelle, C. Petter, J.M. Lopez-Cuesta, Fire retardancy of ethylene vinyl acetate/ultrafine kaolinite composites, Polym. Degrad. Stab. vol. 100 (1) (2014) 54–62, https://doi.org/10.1016/j.polymdegradstab.2013.12.026.

[36] M.C. Costache, D.D. Jiang, C.A. Wilkie, Thermal degradation of ethylene-vinyl acetate coplymer nanocomposites, Polym. (Guildf.) vol. 46 (18) (2005) 6947–6958, https://doi.org/10.1016/j.polymer.2005.05.084.

[37] M. Zanetti, G. Camino, R. Muïhaupt, Combustion behaviour of EVA/fluorohectorite nanocomposites, Polym. Deg Stab. vol. 74 (3) (2001) 413–417, https://doi.org/10.1016/S0141-3910(01)00178-1.

[38] Z. Jiang, C. Hu, S.M. Easa, X. Zheng, Y. Zhang, Evaluation of physical, rheological, and structural properties of vulcanized EVA/SBS modified bitumen, J. Appl. Polym. Sci. vol. 134 (21) (2017), https://doi.org/10.1002/app.44850.

[39] F. Khodkar, N.G. Ebrahimi, Effect of irradiation on mechanical and structural properties of ethylene vinyl acetate copolymers hollow fibers, J. Appl. Polym. Sci. vol. 119 (4) (2011) 2085–2092, https://doi.org/10.1002/app.32926.

[40] M. Zanetti, P. Bracco, L. Costa, Thermal degradation behaviour of PE/clay nanocomposites, Polym. Degrad. Stab. vol. 85 (1) (2004) 657–665, https://doi.org/10.1016/j.polymdegradstab.2004.03.005.

[41] S. Kadi, S. Lellou, K. Marouf-Khelifa, J. Schott, I. Gener-Batonneau, A. Khelifa, Preparation, characterisation and application of thermally treated Algerian halloysite, Microporous Mesoporous Mater. vol. 158 (2012) 47–54, https://doi.org/10.1016/j.micromeso.2012.03.014.

[42] Y. Soudais, L. Moga, J. Blazek, F. Lemort, Coupled DTA-TGA-FT-IR investigation of pyrolytic decomposition of EVA, PVC and cellulose, J. Anal. Appl. Pyrolysis vol. 78 (1) (2007) 46–57, https://doi.org/10.1016/j.jaap.2006.04.005.

[43] B.J. McGrattan, Examining the decomposition of ethylene-vinyl acetate copolymers using TG/GC/IR, Appl. Spectrosc. vol. 48 (12) (1994) 1472–1476, https://doi.org/10.1366/0003702944027750.

[44] A. Marcilla, A. Gómez, and S. Menargues, TG/FTIR study of the thermal pyrolysis of EVA copolymers," in Journal of Analytical and Applied Pyrolysis, Elsevier, 2005, pp. 224–230. doi: 10.1016/j.jaap.2004.09.009.

[45] M. Zanetti, T. Kashiwagi, L. Falqui, G. Camino, Cone calorimeter combustion and gasification studies of polymer layered silicate nanocomposites, Chem. Mater. vol. 14 (2) (2002) 881–887, https://doi.org/10.1021/cm011236k.

[46] S.S. Choi, E. Kim, Analysis of pyrolysis products of ethylene-vinyl acetate coploymer (EVA) using pre-deacetylation, J. Anal. Appl. Pyrolysis vol. 127 (2017) 1–7, https://doi.org/10.1016/j.jaap.2017.09.015.
[47] A. Marcilla, A. Gómez, S. Menargues, R. Ruiz, Pyrolysis of polymers in the presence of a commercial clay, Polym. Degrad. Stab. vol. 88 (3) (2005) 456–460, https://doi.org/10.1016/j.polymdegradstab.2004.11.017.
[48] M.B. Maurin, L.W. Dittert, A.A. Hussain, Thermogravimetric analysis of ethylene-vinyl acetate copolymers with Fourier transform infrared analysis of the pyrolysis products, Thermochim. Acta vol. 186 (1) (1991) 97–102, https://doi.org/10.1016/0040-6031(91)87026-S.
[49] M. Sahnoune, A. Taguet, B. Otazaghine, M. Kaci, J.M. Lopez-Cuesta, Effects of functionalized halloysite on morphology and properties of polyamide-11/SEBS-g-MA blends, Eur. Polym. J. vol. 90 (2017) 418–430, https://doi.org/10.1016/j.eurpolymj.2017.03.008.